PCCP

ROYAL SOCIETY OF CHEMISTRY

PAPER

Cite this: *Phys. Chem. Chem. Phys.*, 2021, **23**, 15292

Atomistic insights into the structure and elasticity of densified 45S5 bioactive glasses

Youssef Ouldhnini, †[a] Achraf Atila, †*[b] Said Ouaskit[c] and Abdellatif Hasnaoui [a]

Received 18th May 2021,
Accepted 23rd June 2021

DOI: 10.1039/d1cp02192c

rsc.li/pccp

Glasses have applications in regenerative medicine due to their bioactivity, enabling interactions with hard and soft tissues. Soda-lime phosphosilicate glasses, such as 45S5, represent a model system of bioactive glasses. Regardless of their importance as bioactive materials, the relationship between the structure, density, and cooling process has not been studied in detail. This hinders further development of glasses as biomaterials. We used molecular dynamics simulations to study the elastic and structural properties of densified 45S5 bioactive glass and liquids over a wide range of densities. We performed a systematic analysis of the glass structure to density relationship to correlate the change in the properties with the structural change to enhance the mechanical properties of bioactive glasses while preserving their bioactive nature. The results show that the glass structure tends to be repolymerized, as indicated by increased network connectivity and a tetrahedral to octahedral polyhedral transition. We were able to tailor the elastic properties while keeping the bioactivity of the glass. The results presented here will provide some guidance to develop bioactive glasses with enhanced mechanical properties.

1 Introduction

The daily activities of humans can be disrupted due to fractures, bone tumours, degenerative cartilage disorders, and periodontal diseases. In this regard, many materials were developed with the potential to replace bone and joint tissue,[1–3] and enter in the therapeutic methods of these pathological symptoms. Among these materials, metal-based materials, such as aluminum, zirconium, and titanium, were shown to be useful as an implant in orthopedic surgery to manufacture prostheses, plates, and other components. These metal-based bioactive materials are known to have a lifetime of around twenty years, and with the increase of the human lifespan, this causes problems if they are damaged before the patient dies, which is a common problem, especially in osteology.[4–6] Hence, developing new biomaterials that satisfy our needs is required.

Bioactive glasses have been shown to be an excellent replacement for metallic bioactive materials. Their biocompatibility with the human body makes them qualified for restorative and regenerative biomedical applications such as orthopedic, dental, maxillofacial implants, and tissue engineering.[7] The first bioactive glass was made in the late 1960s by Hench *et al.*, which was a soda-lime phosphosilicate glass named 45S5. The 45S5 bioactive glass represents a reference in the field of materials for biomedicine. This is due to its excellent biocompatibility with the human body and the absence of an inflammatory response or side effect as well as its ability to form strong bonds with hard and soft tissues, and it facilitates healing and regeneration of injured tissue, especially bones.[6,8,9] The 45S5 bioactive glass is specifically composed of a SiO_2–CaO–Na_2O–P_2O_5 system (46.1 mol%, SiO_2 26.9 mol% CaO, 24.4 mol% Na_2O and 2.6 mol% P_2O_5),[10] and can be an osteoconductive and osteoinductive material as it allows for new bone growth along the bone-implant interface.[11] Furthermore, it is known to establish a strong interface with tissues through chemical reactions. Also, it produces a partial dissolution on its surface, leading to the formation of a phosphocalcium layer.[8,9] The phosphocalcium layer eventually crystallizes into a hydroxy-carbonate apatite (HCA), which has a similar composition to biological hydroxyapatite, the first mineral phase of bones, dental enamel, and dentin.

The bioactivity of these materials is often measured in terms of the rate and ability of HCA crystallization.[12–15] This rate is strongly dependent on the composition and the preparation conditions of the glass.[16–18] The HCA crystallizes very rapidly on the 45S5 bioactive glass surface, mainly due to the low silicate content (45 mol%). It is also worth stressing that when the silica content increases, the bioactivity decreases significantly, which is

[a] *LS3M, Faculté Polydisciplinaire Khouribga, Sultan Moulay Slimane University of Beni Mellal, B.P 145, 25000 Khouribga, Morocco*
[b] *Department of Materials Science Engineering, Institute I: General Materials Properties, Friedrich-Alexander-Universität Erlangen-Nürnberg, 91058 Erlangen, Germany. E-mail: achraf.atila@fau.de, achraf.atila@gmail.com*
[c] *Laboratoire de Physique de la Matière Condensée, Faculté des Sciences Ben M'sik, University Hassan II of Casablanca, B.P 7955, Av Driss El Harti, Sidi Othmane, Casablanca, Morocco*
† Joint first author.

due to the increase in the network polymerization that hinders the HCA crystallization.[19] Moreover, the bioactivity can be associated just with the bone-bonding realization ability of a biomaterial. This behaviour could indicate the material's capability to be compatible with the body.[20] Precisely, the bonding with bones and tissue regeneration ability depends on the ion release rate of soluble species such as calcium, phosphorus, and silicon from the implanted biomaterial glass.[21]

Several previously studied glasses showed high bioactivity (*e.g.*, 58S, S53P4, and 70S30C2)[20,22–24] and highlighted the effect of the glass composition on the bioactivity.[25–27] Ideally, a biomaterial should have both good chemical and mechanical compatibilities with the biological environment where it will be incorporated. Like other properties, mechanical properties are fundamental to understanding how the material will resist the daily loads it will be exposed to. One disadvantage of bioactive glasses is their low mechanical properties (*e.g.*, low strength and fracture toughness). Consequently, the mechanical properties of these glasses are not suitable for supporting stress and load-bearing like natural bones. Preferably in clinical (*e.g.*, dental) applications, the mechanical properties of a bioactive glass implant should appropriately match the host tissue and show strong binding to hard and soft tissues.[28–35]

Computer simulations, such as molecular dynamics (MD), have become increasingly crucial to study the glass properties such as diffusion and elastic properties and obtain atomic-scale mechanisms by analyzing the structure at an atomic level.[36–42] Earlier MD simulation studies on the density effect in sodium silicate glass[43] and vitreous silica[44] showed structural repolymerization. Consequently, these structural changes affected the glass properties. While the elastic moduli of crystalline oxides increase (decrease) with pressure (temperature),[45] the elastic moduli of oxide glasses show different behaviours with pressure (temperature), and depending on these behaviours, can be seen as normal, anomalous, or intermediate glasses. When the elastic properties increase (decrease) with increasing (decreasing) pressure (temperature), the glass is seen as a normal glass,[46,47] anomalous glasses are characterized by a negative (positive) correlation of the elastic moduli with pressure (temperature),[48] and intermediate glasses show an elastic response that is independent of temperature and/or pressure.[45,49]

In this paper, we used MD simulations to systematically investigate the structural and elastic properties of densified 45S5 bioactive glasses. This enabled us to gain an overview of the dependence of the elastic properties and bioactivity on the density. We suggested that controlling the elasticity and bioactivity of these glasses could be achieved by controlling the cooling pressure, which broadens the usage of these bioactive glasses in different implantation zones. The remainder of this paper is arranged as follows: in Section 2 we briefly describe the steps followed to obtain the glasses under different densities and how we computed other properties. In Section 3 we present the effect of density on the structural and elastic properties of 45S5 glasses. In Section 4 we discussed the results in terms of bioactivity. Concluding remarks are given in Section 5.

2 Computational details

In this study, we used the potential developed by Pedone *et al.*[50] that takes into account the oxidation state of atoms and have interatomic potential energy of the form:

$$U(r_{ij}) = \frac{z_i z_j e^2}{r} + D_{ij}\left[\left\{1 - e^{-a_{ij}(r-r_0)}\right\}^2 - 1\right] + \frac{C_{ij}}{r^{12}} \qquad (1)$$

where i and j stand for atoms (Si, O, P, Na, and Ca), r is the distance between atoms i and j, and z_i and z_j are the effective charges of the atoms i and j. D_{ij}, a_{ij}, r_0, and C_{ij} are potential parameters. The first term of the left-hand side in eqn (1) describes the long-range electrostatic interaction between atoms, the second one is a short-range Morse function, which is usually used in modeling bonded interactions in covalent systems, and the last term represents a repulsive contribution, necessary to model the interaction at high temperatures and pressures.[50] This potential reproduces reasonably the structural, elastic, and dynamical properties of a wide range of oxide glasses and has good agreement with available experimental data as mentioned in the literature.[37,38,41,50–58] Potential parameters and partial charges are given in ref. 50. All simulations were performed using the LAMMPS code.[59] Coulomb interactions were evaluated by the Ewald summation method with a cutoff of 12.0 Å and a relative error in forces of 10^{-5}. The short-range interaction cutoff was taken to be 5.5 Å. The simulations were run in the canonical ensemble (*NVT*) using the Nosé–Hoover thermostat.[60–62] The equations of motion were solved using the velocity-Verlet algorithm as implemented in LAMMPS with a timestep of 1 fs. Periodic boundary conditions were applied in all directions to avoid the edge effect.

We randomly placed 4275 atoms in a cubic simulation box while ensuring that there are no overlapping atoms to reproduce the 45S5 nominal molar composition $(CaO)_{26.82}$–$(Na_2O)_{24.39}$–$(SiO_2)_{46.3}$–$(P_2O_5)_{2.44}$. The simulation box length was varied to get different densities ranging from 2.32 g cm^{-3} to 5.71 g cm^{-3}. The system was equilibrated at a high temperature (4000 K) for 500 ps for each box length to reach the equilibrium liquid state. The melt was then quenched to 300 K using a cooling rate of 1 K ps^{-1}, and this very high cooling rate has already been used in several MD studies.[36,38,63] After quenching, the glass was further equilibrated at 300 K in the *NVT* ensemble for 1.5 ns. All the results presented in this paper are averaged over 500 configurations (over the last 500 ps of the *NVT* run) to get statistically meaningful results. The room temperature experimental glass density[63] of 2.7 g cm^{-3} is obtained with L = 38.5 Å. The pressure at this density is around $P = -0.023$ GPa, which is negligible, and we can say that the potential used in this study gives a realistic glass.

2.1 Elastic properties

In order to calculate the elastic properties, we refer to the second derivative method.[37] This method can be used to obtain the stiffness matrix as well as the compliance matrix. Using a

single-point energy calculation, the stiffness matrix elements are obtained by:

$$C_{ij} = \frac{1}{V}\frac{\partial^2 U}{\partial \varepsilon_\alpha \partial \varepsilon_\beta} \quad (2)$$

For an isotropic cubic material, there is only two independent parameters of the stiffness matrix (C_{11} and C_{44})[37,50] and following the Voigt convention, the bulk, shear and Young's moduli can be calculated from eqn (3)–(5) while the Poisson ratio is given by eqn (6).

$$B_{\text{Voigt}} = \frac{1}{9}(C_{11} + C_{22} + C_{33} + 2(C_{12} + C_{13} + C_{23})) \quad (3)$$

$$G_{\text{Voigt}} = \frac{1}{15}(C_{11} + C_{22} + C_{33} + 3(C_{44} + C_{55} + C_{66}) - C_{12} - C_{13} - C_{23}) \quad (4)$$

$$E = \frac{9BG}{3B + G} \quad (5)$$

$$\nu = \frac{E}{2G} - 1 \quad (6)$$

The obtained mechanical properties reported in this paper were calculated using molecular statics through energy minimization. The obtained glass structures at 300 K were subjected to an energy minimization to the closest energy minimum in the potential energy landscape using the conjugate gradient algorithm. The minimized structures were deformed in each of the six directions in both positive and negative directions, and the stress tensor was measured.

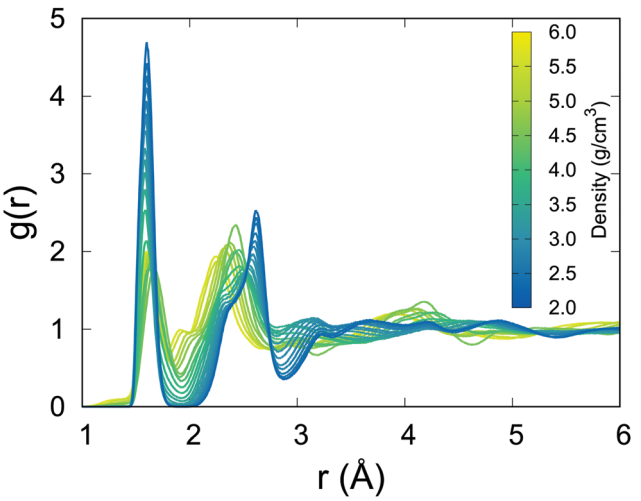

Fig. 1 Total radial distribution function at 300 K obtained from our MD simulations of 45S5 bioactive glass at different densities.

3 Results

3.1 Radial distribution functions

The total radial distribution function (RDF) at different densities is shown in Fig. 1. As depicted in this figure, we noticed that the total RDF's first peak tends to shift to larger distances with increasing density. As the density increases, the intensity of the first peak decreases while it becomes broader compared to the glasses with lower densities. Otherwise, the second peak of the total RDF shifts to a lower distance and becomes broader. It is also worth stressing that the first peak of the total RDF corresponds to the P–O and Si–O pairs, while that of the other pairs is mainly starting from distances larger than 2 Å (see below). At lower densities, it is noticed that the total RDF's first minimum is almost equal to 0, while with increasing density, this value tends to increase, which suggests a slight overlapping between the first and second peaks. Compared to available experimental results for the room temperature and ambient pressure of 45S5 bioactive glass,[64] the total RDF obtained by our molecular dynamics simulation is in good agreement.

Fig. 2 depicts the Si/P–O pair distribution functions as a function of the density at 300 K; these distributions show a significant change during the density increase. At ambient glass density, the shape of these pair distribution functions and the

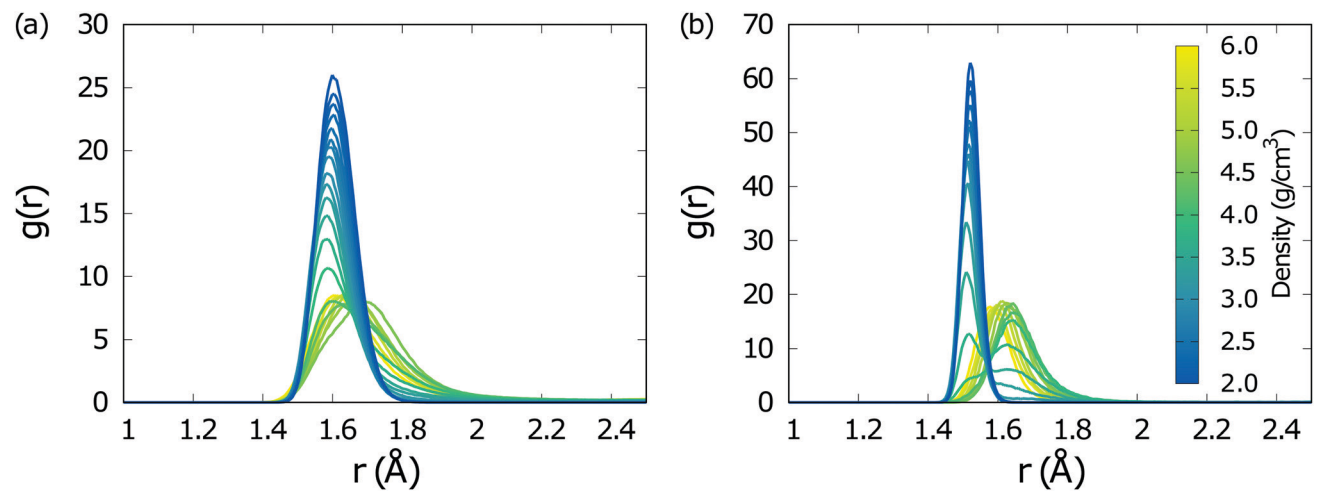

Fig. 2 Partial pair distribution functions at different densities of 45S5 bioactive glasses at 300 K. (a) Si–O and (b) P–O.

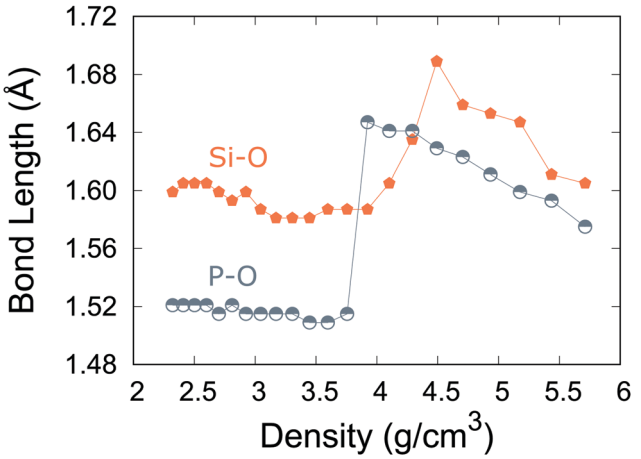

Fig. 3 Si–O and P–O mean bond lengths as a function of the density at 300 K in the simulated 45S5 bioactive glass. Error bars are smaller than the symbol size.

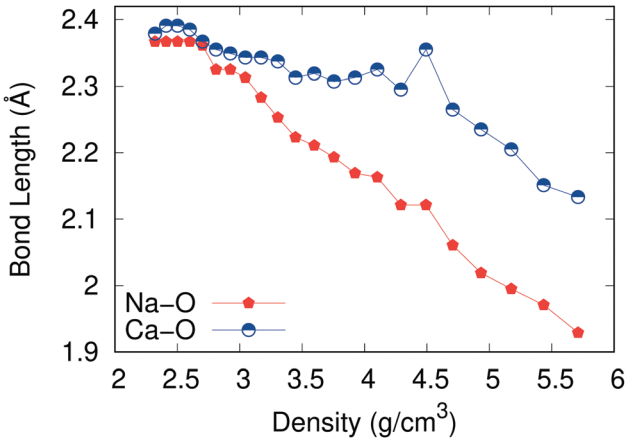

Fig. 5 (a) Na–O and Ca–O bond lengths as a function of the 45S5 bioactive glass density at 300 K. Error bars are smaller than the symbol size.

peak positions are in excellent agreement with previously reported results from MD simulations.[65] The positions of the first peaks in $g_{Si-O}(r)$ and $g_{P-O}(r)$ slightly decrease with increasing density up to a density around 4 g cm^{-3}. We observed a sudden increase in the bond length at densities higher than 4 g cm^{-3} for both Si–O and P–O. A decrease follows this jump in these bond lengths (see Fig. 3).

Fig. 4 displays changes in the Na–O and Ca–O pair distribution function with increasing density. The first peaks for the Na–O Ca–O pairs continuously decrease with increasing density. At a density of 2.32 g cm^{-3}, the nearest-neighbor Na–O and Ca–O separations are 2.36 Å and 2.379 Å, respectively. When the glass density increases and reaches 5.55 g cm^{-3}, these peak positions decrease to 1.929 Å and 2.133 Å, respectively, as shown in Fig. 5. Additionally, the Na–O bond length decreased with a rate higher than that of the Ca–O bond.

3.2 Coordination numbers

The evolution of the Si and P coordination numbers with density are depicted in Fig. 6(a and b). These coordination states can be found by counting the number of oxygens in the first coordination shell, which is indicated by a sphere with a radius corresponding to the first minimum in the pair distribution function. With increasing density, the fraction of Si^4 (silicon tetrahedra) atoms remains constant up to a density around 3.5 g cm^{-3} where it starts to decrease. At the same density, the fraction of Si^5 (silicon pendahedra) atoms begins to increase and reaches a maximum at a density close to 4.25 g cm^{-3} before a continuous decrease as density increases. The fraction of Si^6 (silicon octahedra) atoms increases significantly and continuously from 3.5 g cm^{-3} to a maximum value at 5.71 g cm^{-3} and becomes the dominant coordination state. The fraction of P^4 (phosphorous tetrahedra) atoms decreases sharply from 3.3 g cm^{-3} until it disappears at a density around 4 g cm^{-3}. The P^5 reaches a maximum at a density around 3.75 g cm^{-3} then continuously decreases as density increases. The P^6 fraction keeps increasing with the density and becomes the only phosphorous coordination state at the highest density studied here.

The oxygen species were identified based on the total number of bonds to Si or P atoms. Therefore, O^0, O^1, O^2, and

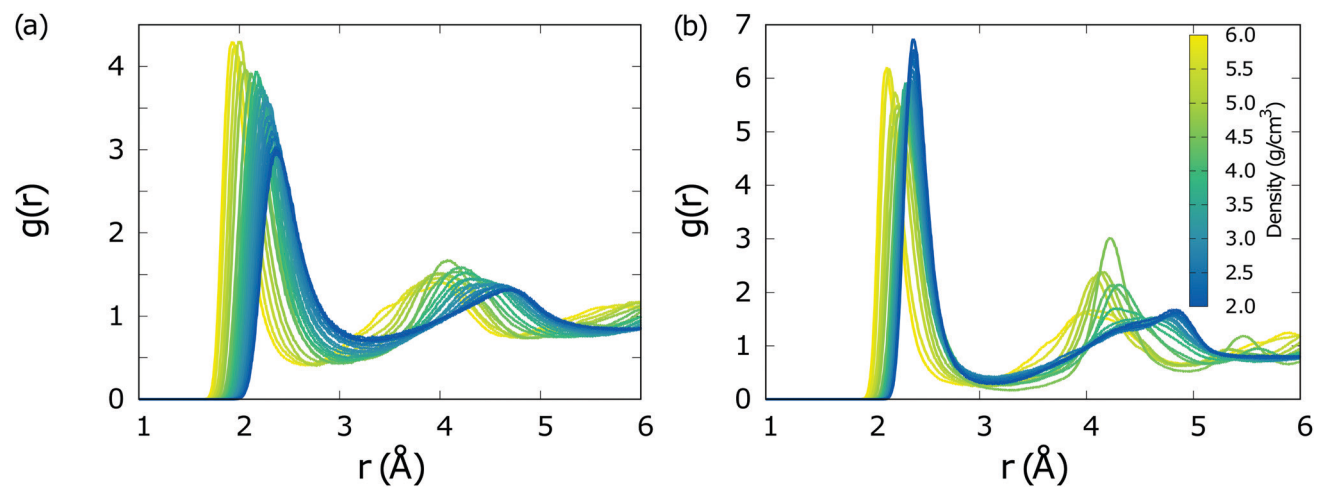

Fig. 4 Partial pair distribution functions for different densities of 45S5 bioactive glasses at 300 K. (a) Na–O and (b) Ca–O.

O^3 indicate free oxygen (FO), nonbridging oxygen (NBO), bridging oxygen (BO), and oxygen tricluster (TBO), which is oxygen linked to three network former atoms. The distributions of these oxygen species are shown in Fig. 6(c). The population of NBO is dominant as expected from the composition of the glass, and it is in good agreement with previous studies.[64] Additionally, at a density around 3.5 g cm^{-3} the fraction of O^2 atoms begins to increase while that of O^1 decreases. Also, the population of O^2 atoms reaches a maximum at a density around 4.6 g cm^{-3} and decreases with further density increase. Moreover, at a density around 4.5 g cm^{-3} the fraction of triclusters increases.

3.3 Bond angle distributions

We used the bond-angle distribution (BAD) to get quantitative information about the bond angles (*e.g.*, O–Si–O). Fig. 7(a and b) display the distribution of O–Si–O and O–P–O bond angles for

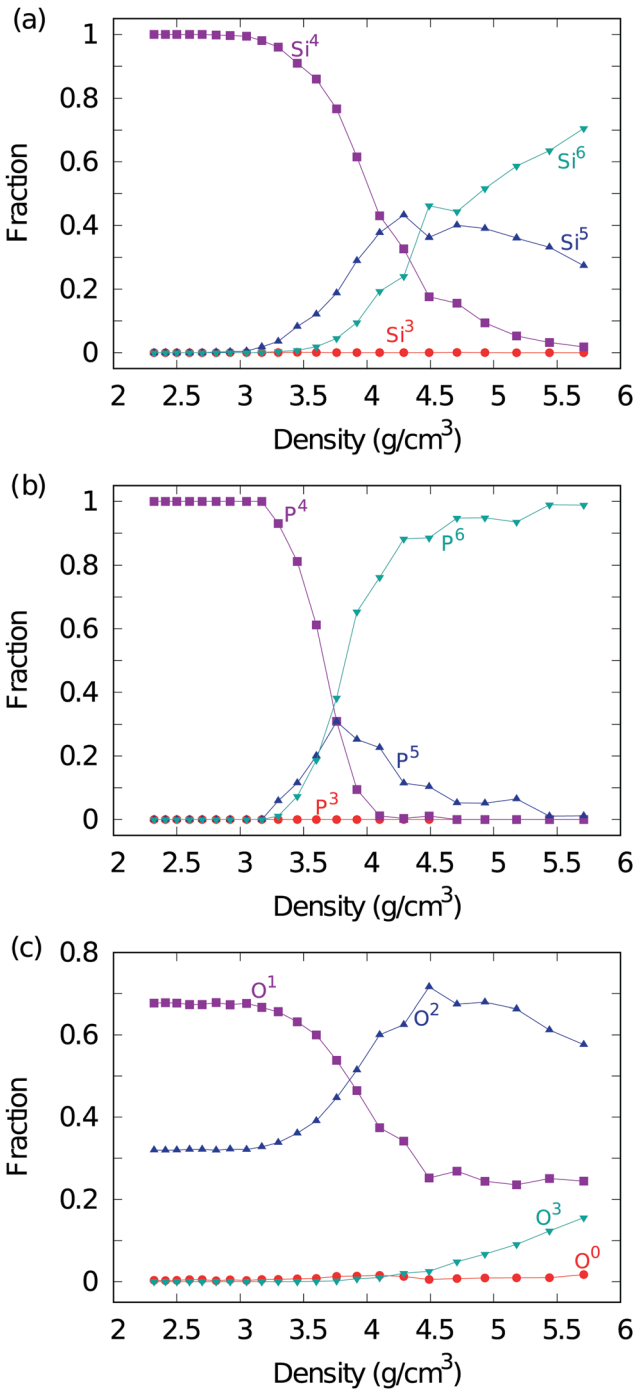

Fig. 6 Coordination numbers and oxygen species as a function of the density. (a) Si–O coordination numbers, (b) P–O coordination numbers, (c) oxygen species, and (d) Q^n distribution. Error bars are smaller than the symbol size.

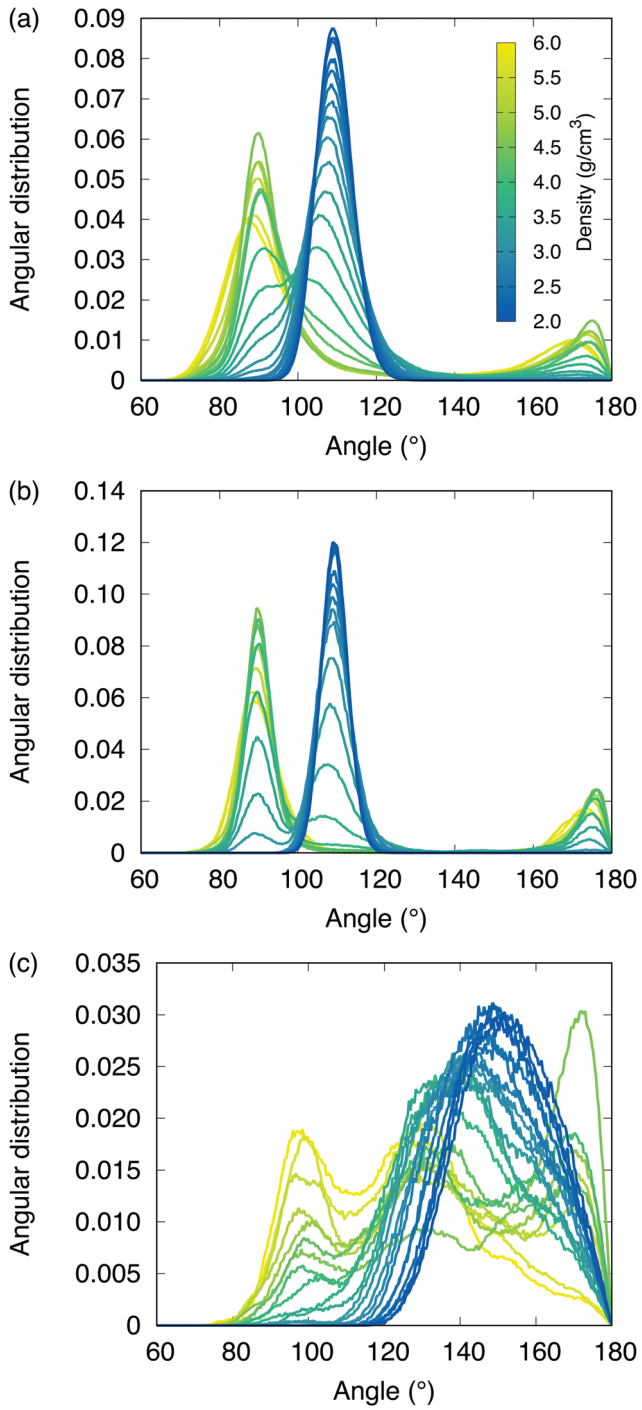

Fig. 7 Bond angle distributions under densification obtained from MD simulations at 300 K. (a) O–Si–O, (b) O–P–O, and (c) Si–O–Si.

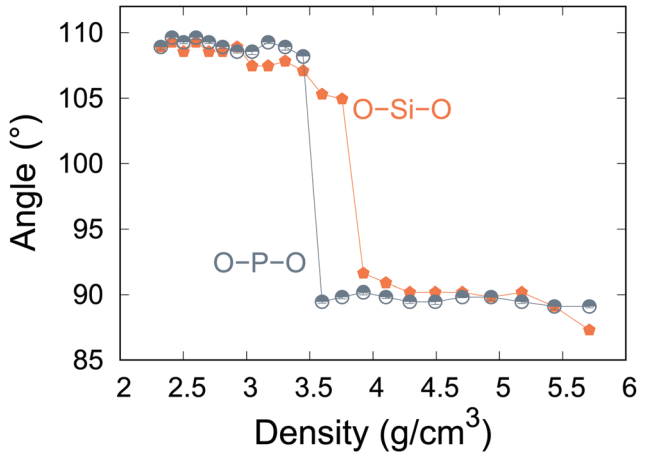

Fig. 8 O–Si–O and O–P–O angles at the maximum intensity of the BAD as a function of the density. Error bars are smaller than the symbol size.

different densities. At low densities, the O–Si–O and O–P–O BADs show only one well-defined peak, at an angle around 108.9°, which is very close to the perfect tetrahedral angle 109.5°. As the density increases, the peaks of the O–Si–O and O–P–O BADs become broader and shift to lower angles around $\theta_{\text{O–Si–O}}$ = 87.3° and $\theta_{\text{O–P–O}}$ = 89.1°, respectively. Additionally, smaller peaks closer to an angle of 180° start to be observed. Besides, the Si–O–Si bond angle distribution represents the angle between two tetrahedra. In Fig. 7(c) at lower densities, the Si–O–Si bond-angle distribution has a single peak centered around 149°. With the density increase, the peak decreases to an angle around 87°. Fig. 8 depicts the evolution of the O–Si/P–O angles with the density. The variation of the mean bond angle of these angles shows similar behavior. They both decrease slightly up to densities around 3.6 g cm^{-3} where they decrease dramatically. After that, the mean bond angle continues decreasing slightly.

3.4 Q^n distribution

The medium-range structure and connectivity of the glass structure are studied using the Q^n distribution. The n indicates the number of bridging oxygens in each silicon and/or phosphorous tetrahedra. Fig. 9(a) shows the evolution of the Q^n populations with density; at densities lower than 3.5 g cm^{-3} there are small fluctuations in the population of these species. At densities higher than 3.5 g cm^{-3}, the Q^0, Q^1, Q^2, and Q^3 fractions start to decrease, while there is an increase in Q^5, which reaches a maximum at 5.25 g cm^{-3}. The Q^6 population starts to grow up from 3.75 g cm^{-3}.

The network connectivity (NC) is calculated using $\text{NC} = \sum_{n=1}^{n} 4x_n$, where x_n is the fraction of the Q^n (with n = 1, 2, 3, 4, 5, or 6). The NC is the average number of BOs in Si and/or P's first coordination shell. For the 45S5 glass, it is known that the NC is 2, which is consistent with the calculated value in our study, as can be seen in Fig. 9(b). The NC is constant and equal to two up to densities around 3.5 g cm^{-3}. With further increase of the density, the NC keeps increasing, and at densities larger than 4.5 g cm^{-3} it shows a plateau at a value around NC = 5.

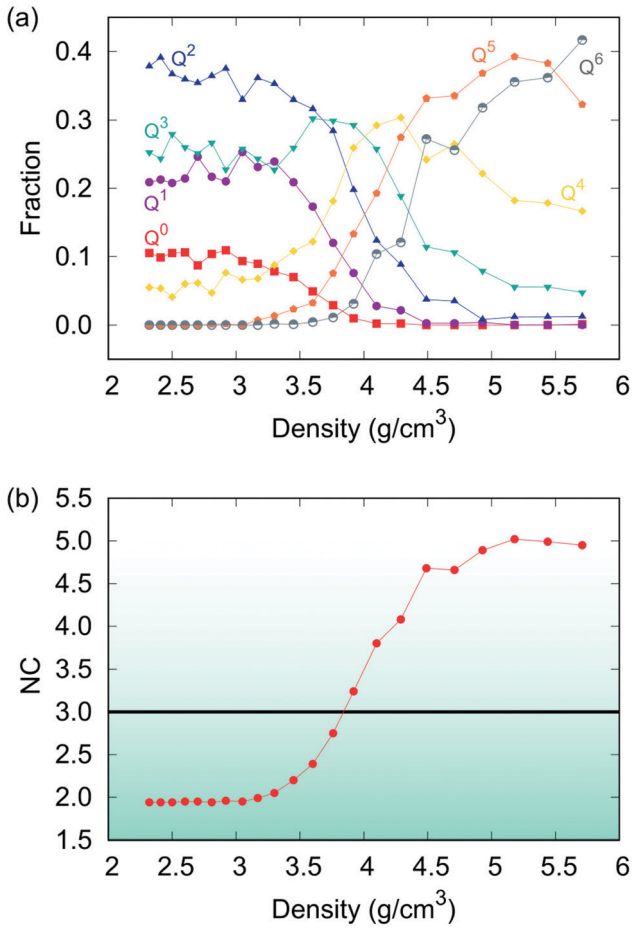

Fig. 9 (a) Q^n distribution and (b) network connectivity as a function of the density. Error bars are smaller than the symbol size.

3.5 Elastic properties

Fig. 10 displays the evolution of the Young, bulk, and shear moduli with density. When the density increases, we see that there is an increase in the elastic moduli. This behavior of the elastic moduli is consistent with previous studies of other glasses.[66] The rate of this increase is low, up to 2.75 g cm^{-3}

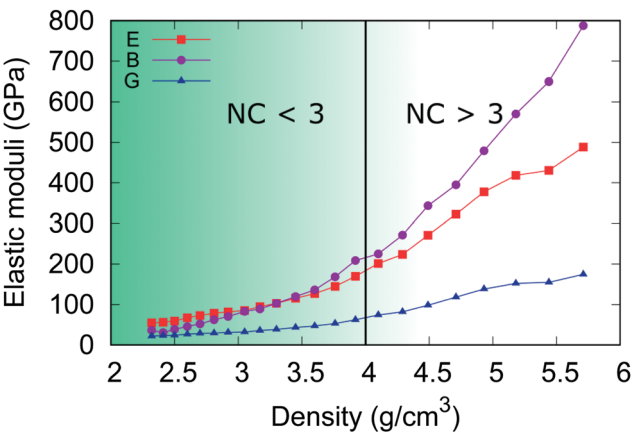

Fig. 10 Elastic moduli as a function of the density.

for both the Young and bulk moduli; the bulk modulus showing a more significant increase with density. It increases from 22 GPa in the glass with the lowest density to 787 GPa in the glass with the highest density. The young modulus increases from 55 GPa for the lowest density of the 45S5 glass to 488 GPa for the glass with the highest density. Also, the shear modulus increased but slower compared to the bulk and Young's moduli.

4 Discussion

In the 45S5 glass simulated in this study, we observed a tetrahedral to octahedral transition as indicated by the sudden change in the Si/P–O bond lengths and the O–Si/P–O bond angles as the density increases. First of all, the initial decrease of the bond length is due to decreased SiO_4 and PO_4 tetrahedra size. The constant coordination numbers of Si and P atoms in the same density range support this fact. Moreover, the O–Si/P–O angles are also a further indication that there is shrinking of the tetrahedra's size in the same density regions. Secondly, the transition regime is characterized by a sudden increase of the Si/P–O bond lengths accompanied by a smoother change in the Si and P coordination numbers indicated by the coexistence of Si^n and P^n (n = 4, 5, 6). The sudden drop in the O–Si/P–O angles to values around 90°, which is the characteristic angle of an octahedron, occurs in the same density region. An additional signature for this transition is seen from the increasing peak at 180°, which appears for larger densities. These findings were also observed in previous simulations and experiments of silicate glasses.[67–70]

If we focus on the glass modifiers (Na and Ca), we only observe a continuous decrease in the Na/Ca–O bond lengths with increasing density. The rate of this decrease is higher for Na–O than Ca–O bond lengths. The decrease of the Na–O bond distance with pressure has also been observed in experiments using nuclear magnetic resonance by Lee[71] and previous MD simulations.[43] The difference in the decreasing rate between Na–O and Ca–O bonds is explained by the fact that the field strength of the Na–O bond is lower than that of the Ca–O bond.[37] The field strength (field strength $= \frac{z_C}{(r_C + r_O)^2}$, where z_C is the cation valence, r_C is the cation radius, and r_O is the oxygen radius) indicates the degree of covalency of the bonds; higher field strength means higher covalency of the bond (higher bond strength and more directionality). Based on this definition, it is evident that Na–O bonds are more sensitive to pressure and will show greater change compared to that of the Ca–O bond. Similar behaviour was reported experimentally in modified silicate[68] and aluminosilicate[72,73] glasses and melts under pressure.

The oxygen species were also affected by the density change. The change of the oxygen population can be divided into three regimes: (I) in the range of density less than 3 g cm^{-3}, the fractions of all oxygen types are constant, which is due to the constant coordination numbers of both Si and P in that regime. (II) For density ranging between 3 and 4.5 g cm^{-3}, we observe a decrease of the NBO population accompanied by an increase in the BO population. (III) At densities larger than 4.5 g cm^{-3} there is an increase of oxygen triclusters at the expense of BO. These oxygen population changes indicate a repolymerization of the network by creating density-induced BO and TBO at the expense of NBO. We want to stress that TBO atoms were found in previous studies in other glasses.[36,37]

As stated before, the changes within the glass network can also be seen through the Q^n distribution. At ambient pressure conditions, the Q^n distribution usually depends on the glass composition and can go from Q^4 for the case of silica to Q^0 for a fully depolymerized glass. Moreover, for other glasses such as ternary aluminosilicate glasses, Q^5 and Q^6 are found in smaller amounts.[36,37] The changes in the Q^n are directly correlated with the changes in the silicon, phosphorous, and oxygen coordination numbers. The changes in the Q^n distribution influence glass properties, such as bioactivity and mechanical properties. At ambient density (ρ = 2.7 g cm^{-3}) there is a predominance of Q^2 units, besides a significant amount of Q^1 with some degree of cross-linking provided by Q^3 species and a negligible amount of Q^4 and Q^0. These findings are similar to what has been observed experimentally by Raman spectroscopy and NMR spectroscopy[74,75] and in good agreement with CPMD simulation obtained by Tilocca *et al.*[65] It was also shown experimentally that the 45S5 glass structure at ambient pressure and density is made of Q^0, Q^2, and Q^3 units.[64]

The bioactivity of melt-quenched bioactive glass depends on the composition; as for the 45S5 glass, there is a high content of modifiers, small phosphorus content, and a structure mainly made of silicon atoms as a dominant network forming element. In the literature, the silicate network's polymerization degree is seen as an important parameter to assess the bioactivity of silicate glasses.[8,9,76–79] This parameter can be calculated from the structure obtained by MD simulations.[80,81] The value of this network connectivity should be less than 3 for an excellent bioactive glass. The value of the network connectivity for the 45S5 bioactive glass is around 2. Thus, changing the density in a way that leads to an increase of the elastic moduli while keeping the network connectivity less than 3 is a promising way to enhance the elasticity and mechanical properties of bioactive glasses without losing their bioactive nature. The network connectivity as calculated from our simulated glasses is consistent with the experimental observations.[80,81] As expected from the changes in the Si, P, and O coordination numbers, the NC increased with increasing density. The NC reaches a value of 3 at a density around 4 g cm^{-3}. We can consider glasses below this threshold as bioactive ones, while those obtained for densities larger than 4 g cm^{-3} as bio-inactive glasses. These observations are consistent with previous *in vitro* studies that focused on changing the glass network connectivity through composition design and lead to similar conclusions.[82–84] In addition to that, earlier experimental studies on the pressure effect on the dissolution behaviour and glass structure of phosphate and silicate-based glasses[85] showed that hot compression affects the dissolution kinetics of these glasses, which was correlated to an increase of the coordination and number of constraints of atoms.[85] These findings highlighted the importance of glass topology in controlling the

dissolution kinetics[85] and are in line with our conclusions and further support our results. Moreover, it was shown previously that an increase of the elastic moduli was positively correlated to an increase in the network connectivity,[36,86] and the F_{net}, which is a parameter that takes into account both structural and energetic properties of the glass, showed that the network connectivity increases with increasing F_{net}.[39,86–89]

This work aimed to enhance the mechanical properties of the 45S5 glass while maintaining its bioactive nature. This was achieved by increasing the density up to 4 g cm^{-3}, which has led to an increase of elastic moduli by more than 230% as illustrated in Fig. 10, while the connectivity remained lower than 3. The increase of the elastic moduli with increasing density is due to the repolymerization of the structure and by the change in the nature of bonding within the glass structure. The Si and P atoms showed a tetrahedral to octahedral transition along with an increase of the BO and TBO. These changes indeed affect the bonding energies of the X–O bonds (X = Si, P, Na, or Ca).

The results suggest that the mechanical properties of bioactive glasses can be enhanced by cooling the glass under pressure. Our findings provide more insights into the relationship between the thermodynamic condition used to prepare the glass and its structural and mechanical properties. The obtained bioactive glasses in this study can be used in a wide range of densities depending on the required elastic moduli. Having a bioactive glass that is mechanically compatible with bones, such as a vertebral column, as *in vivo* applications, can offer an alternative to bioactive ceramic A/W (cerabone), which has a Young's modulus of 118 GPa. The cerabone Young's modulus is higher than that of the 45S5 bioactive glass with ambient pressure. However, the 45S5 bioactive glass with a density around 3.45 g cm^{-3} shows a Young's modulus of 115 GPa[20,74] and hence can be used for this replacement still with a good enough biocompatibility suggested by a network connectivity less than 3 (see Fig. 9 and 10). More studies are needed to test our proposed methodology quantitatively and to apply it to other bioactive glasses. Moreover, the optimal density range provided in this paper might change under experimental conditions and needs to be confirmed.

5 Conclusions

In conclusion, we performed molecular dynamics simulations to investigate the structure and properties of 45S5 glass with various densities. A tetrahedral to octahedral transition for both Si and P atoms was observed. The oxygen species showed a significant change as indicated by a decrease of the NBO fraction and an increase of the BO and TBO fractions with increasing density. These changes indicate the repolymerization of the network with increasing density. Additionally, the glass network connectivity was affected by the density change, which caused a change in the glass bioactivity. The novel aspect of our simulations is the presence of a bioactive to bio-inactive transition, which was ultimately linked to the tetrahedral to octahedral transition and the glass network repolymerization. The increase in the elastic moduli with increasing density supports our hypothesis suggesting that the mechanical properties can be enhanced by cooling the glass under pressure. A density range where there is a significant increase in the elastic moduli while the bioactivity is slightly affected was highlighted. Altogether the results presented in this paper will deepen our understanding of the effect of pressure and high-temperature densification on the structure–bioactivity–elasticity in bioactive oxide glasses. The insight given here will hold for all normal bioactive oxide glasses and pave a new route towards the design of functional bioactive glasses with controlled properties.

Conflicts of interest

There are no conflicts to declare.

Acknowledgements

A. Atila thanks the German Research Foundation (DFG) for financial support through the priority program SPP 1594 – Topological Engineering of Ultra-Strong Glasses. The authors gratefully acknowledge the computing resources provided by the Erlangen Regional Computing Center (RRZE) for running some of the simulations.

References

1 M. Shahgholi, S. Oliviero, F. Baino, C. Vitale-Brovarone, D. Gastaldi and P. Vena, *J. Eur. Ceram. Soc.*, 2016, **36**, 2403–2409.
2 S. Midha, T. B. Kim, W. van den Bergh, P. D. Lee, J. R. Jones and C. A. Mitchell, *Acta Biomater.*, 2013, **9**, 9169–9182.
3 X.-s. Wang, Z.-l. Lu, L. Jia and J.-x. Chen, *J. Iron Steel Res. Int.*, 2017, **24**, 97–102.
4 L. Hench, J. Polak, I. Xynos and L. Buttery, *Mater. Res. Innovations*, 2000, **3**, 313–323.
5 L. L. Hench and J. R. Jones, *Front. Bioeng. Biotechnol.*, 2015, **3**, 194.
6 L. L. Hench, *J. Eur. Ceram. Soc.*, 2009, **29**, 1257–1265.
7 L. L. Hench and J. Wilson, *Science*, 1984, **226**, 630–636.
8 L. L. Hench, R. J. Splinter, W. Allen and T. Greenlee, *J. Biomed. Mater. Res.*, 1971, **5**, 117–141.
9 L. L. Hench, *J. Am. Ceram. Soc.*, 1991, **74**, 1487–1510.
10 M. N. Rahaman, D. E. Day, B. S. Bal, Q. Fu, S. B. Jung, L. F. Bonewald and A. P. Tomsia, *Acta Biomater.*, 2011, **7**, 2355–2373.
11 A. R. Boccaccini and J. J. Blaker, *Expert Rev. Med. Devices*, 2005, **2**, 303–317.
12 A. Martinez, I. Izquierdo-Barba and M. Vallet-Regi, *Chem. Mater.*, 2000, **12**, 3080–3088.
13 J. Oliveira, R. Correia and M. Fernandes, *Biomaterials*, 2002, **23**, 371–379.
14 M. Cerruti, C. L. Bianchi, F. Bonino, A. Damin, A. Perardi and C. Morterra, *J. Phys. Chem. B*, 2005, **109**, 14496–14505.
15 Q. Chen, J. Roether and A. Boccaccini, *Top. Tissue Eng.*, 2008, **4**, 1–27.

16 K. S. Lin, Y.-H. Tseng, Y. Mou, Y.-C. Hsu, C.-M. Yang and J. C. Chan, *Chem. Mater.*, 2005, **17**, 4493–4501.
17 M. Vallet-Regi and A. Rámila, *Chem. Mater.*, 2000, **12**, 961–965.
18 H. Yan, K. Zhang, C. F. Blanford, L. F. Francis and A. Stein, *Chem. Mater.*, 2001, **13**, 1374–1382.
19 L. L. Hench and J. Wilson, *An Introduction to Bioceramics*, World Scientific, 1993.
20 J. R. Jones, *Acta Biomater.*, 2013, **9**, 4457–4486.
21 L. L. Hench, *J. Mater. Sci.: Mater. Med.*, 2006, **17**, 967–978.
22 P. Sepulveda, J. R. Jones and L. L. Hench, *J. Biomed. Mater. Res.*, 2002, **61**, 301–311.
23 P. Stoor, E. Söderling and J. I. Salonen, *Acta Odontol. Scand.*, 1998, **56**, 161–165.
24 M. Brink, T. Turunen, R.-P. Happonen and A. Yli-Urpo, *J. Biomed. Mater. Res.*, 1997, **37**, 114–121.
25 E. Zeimaran, S. Pourshahrestani, I. Djordjevic, B. Pingguan-Murphy, N. A. Kadri and M. R. Towler, *Mater. Sci. Eng., C*, 2015, **53**, 175–188.
26 A. A. Gorustovich, J. A. Roether and A. R. Boccaccini, *Tissue Eng., Part B*, 2010, **16**, 199–207.
27 Y. Xiang and J. Du, *Chem. Mater.*, 2011, **23**, 2703–2717.
28 R. Shah, A. Sinanan, J. Knowles, N. Hunt and M. Lewis, *Biomaterials*, 2005, **26**, 1497–1505.
29 H. Shin, S. Jo and A. G. Mikos, *Biomaterials*, 2003, **24**, 4353–4364.
30 Q.-Z. Chen, S. E. Harding, N. N. Ali, A. R. Lyon and A. R. Boccaccini, *Mater. Sci. Eng., R*, 2008, **59**, 1–37.
31 S. Minardi, B. Corradetti, F. Taraballi, M. Sandri, J. Van Eps, F. J. Cabrera, B. K. Weiner, A. Tampieri and E. Tasciotti, *Biomaterials*, 2015, **62**, 128–137.
32 P. Ducheyne and Q. Qiu, *Biomaterials*, 1999, **20**, 2287–2303.
33 H. H. Lu, S. F. El-Amin, K. D. Scott and C. T. Laurencin, *J. Biomed. Mater. Res.*, 2003, **64A**, 465–474.
34 S.-S. Kim, K.-M. Ahn, M. S. Park, J.-H. Lee, C. Y. Choi and B.-S. Kim, *J. Biomed. Mater. Res., Part A*, 2007, **80A**, 206–215.
35 R. M. Day, A. R. Boccaccini, S. Shurey, J. A. Roether, A. Forbes, L. L. Hench and S. M. Gabe, *Biomaterials*, 2004, **25**, 5857–5866.
36 A. Atila, E. M. Ghardi, A. Hasnaoui and S. Ouaskit, *J. Non-Cryst. Solids*, 2019, **525**, 119470.
37 A. Atila, E. M. Ghardi, S. Ouaskit and A. Hasnaoui, *Phys. Rev. B*, 2019, **100**, 144109.
38 A. Atila, S. Ouaskit and A. Hasnaoui, *Phys. Chem. Chem. Phys.*, 2020, **22**, 17205–17212.
39 A. Atila, M. Kbirou, S. Ouaskit and A. Hasnaoui, *J. Non-Cryst. Solids*, 2020, **550**, 120381.
40 A. Atila, arXiv preprint, arXiv:2007.09247, 2020.
41 E. M. Ghardi, A. Atila, M. Badawi, A. Hasnaoui and S. Ouaskit, *J. Am. Ceram. Soc.*, 2019, **102**, 6626–6639.
42 A. Tilocca, *Proc. R. Soc. London, Ser. A*, 2009, **465**, 1003–1027.
43 M. Bauchy, *J. Chem. Phys.*, 2012, **137**, 044510.
44 S. T. John, D. D. Klug and Y. Le Page, *Phys. Rev. B: Condens. Matter Mater. Phys.*, 1992, **46**, 5933.
45 S. P. Jaccani, S. Sundararaman and L. Huang, *J. Am. Ceram. Soc.*, 2018, **102**, 1137–1149.
46 S. N. Tkachev, M. H. Manghnani and Q. Williams, *Phys. Rev. Lett.*, 2005, **95**(5), 057402.
47 L. Duffrène, R. Gy, J. E. Masnik, J. Kieffer and J. D. Bass, *J. Am. Ceram. Soc.*, 2005, **81**, 1278–1284.
48 L. Huang, F. Yuan, M. Guerette, Q. Zhao and S. Sundararaman, *J. Mater. Res.*, 2016, **32**, 174–182.
49 G. Scannell, A. Koike and L. Huang, *J. Non-Cryst. Solids*, 2016, **447**, 238–247.
50 A. Pedone, G. Malavasi, M. C. Menziani, A. N. Cormack and U. Segre, *J. Phys. Chem. B*, 2006, **110**, 11780–11795.
51 Y. Yu, M. Wang, N. M. Anoop Krishnan, M. M. Smedskjaer, K. Deenamma Vargheese, J. C. Mauro, M. Balonis and M. Bauchy, *J. Non-Cryst. Solids*, 2018, **489**, 16–21.
52 A. Pedone, G. Malavasi, M. Cristina Menziani, U. Segre and A. N. Cormack, *Chem. Mater.*, 2008, **20**, 4356–4366.
53 A. Pedone, G. Malavasi, A. N. Cormack, U. Segre and M. C. Menziani, *Theor. Chem. Acc.*, 2008, **120**, 557–564.
54 J. Turlier, S. Chaussedent, P. Raso, X. Bidault, M. Vermillac, A. Mehdi, D. Neuville, W. Blanc, N. Gaumer, D. Guichaoua and H. Fneich, *Fiber Lasers Glas. Photonics Mater. through Appl.*, 2018, p. 103.
55 J. Luo, K. Deenamma Vargheese, A. Tandia, J. T. Harris and J. C. Mauro, *J. Non-Cryst. Solids*, 2016, **452**, 297–306.
56 Y. Onodera, Y. Takimoto, H. Hijiya, T. Taniguchi, S. Urata, S. Inaba, S. Fujita, I. Obayashi, Y. Hiraoka and S. Kohara, *NPG Asia Mater.*, 2019, **11**, 75.
57 V. V. Le and H. T. Dinh, *J. Non-Cryst. Solids*, 2020, **530**, 119815.
58 B. Deng, J. Luo, J. T. Harris, C. M. Smith and M. E. McKenzie, *J. Am. Ceram. Soc.*, 2019, **103**, 965–972.
59 S. Plimpton, *J. Comput. Phys.*, 1995, **117**, 1–19.
60 W. G. Hoover, *Phys. Rev. A: At., Mol., Opt. Phys.*, 1985, **31**, 1695–1697.
61 S. Nosé, *J. Chem. Phys.*, 1984, **81**, 511–519.
62 M. Parrinello and A. Rahman, *J. Appl. Phys.*, 1981, **52**, 7182–7190.
63 Y. Xiang and J. Du, *Chem. Mater.*, 2011, **23**, 2703–2717.
64 P. Bhaskar, R. Kumar, Y. Maurya, R. Ravinder, A. R. Allu, S. Das, N. N. Gosvami, R. E. Youngman, M. S. Bødker, N. Mascaraque, M. M. Smedskjaer, M. Bauchy and N. A. Krishnan, *J. Non-Cryst. Solids*, 2020, **534**, 119952.
65 A. Tilocca and N. H. de Leeuw, *J. Phys. Chem. B*, 2006, **110**, 25810–25816.
66 C. Weigel, M. Mebarki, S. Clément, R. Vacher, M. Foret and B. Rufflé, *Phys. Rev. B*, 2019, **100**, 094102.
67 A. Zeidler, K. Wezka, R. F. Rowlands, D. A. Whittaker, P. S. Salmon, A. Polidori, J. W. Drewitt, S. Klotz, H. E. Fischer and M. C. Wilding, *et al.*, *Phys. Rev. Lett.*, 2014, **113**, 135501.
68 J. F. Stebbins and S. Bista, *J. Non-Cryst. Solids*, 2019, **505**, 234–240.
69 S. Kapoor, L. Wondraczek and M. M. Smedskjaer, *Front. Mater.*, 2017, **4**, 1.
70 R. G. D. Valle and E. Venuti, *Phys. Rev. B: Condens. Matter Mater. Phys.*, 1996, **54**, 3809–3816.
71 S. K. Lee, *J. Phys. Chem. B*, 2004, **108**, 5889–5900.
72 J. R. Allwardt, J. F. Stebbins, H. Terasaki, L.-S. Du, D. J. Frost, A. C. Withers, M. M. Hirschmann, A. Suzuki and E. Ohtani, *Am. Mineral.*, 2007, **92**, 1093–1104.

73 K. E. Kelsey, J. F. Stebbins, D. M. Singer, G. E. Brown, J. L. Mosenfelder and P. D. Asimow, *Geochim. Cosmochim. Acta*, 2009, **73**, 3914–3933.
74 C.-C. Lin, L.-C. Huang and P. Shen, *J. Non-Cryst. Solids*, 2005, **351**, 3195–3203.
75 A. Pedone, T. Charpentier, G. Malavasi and M. C. Menziani, *Chem. Mater.*, 2010, **22**, 5644–5652.
76 M. Odonnell, S. Watts, R. Law and R. Hill, *J. Non-Cryst. Solids*, 2008, **354**, 3554–3560.
77 Ö. H. Andersson and K. H. Karlsson, *J. Non-Cryst. Solids*, 1991, **129**, 145–151.
78 C. Ohtsuki, T. Kokubo and T. Yamamuro, *J. Non-Cryst. Solids*, 1992, **143**, 84–92.
79 M. ODonnell, S. Watts, R. Hill and R. Law, *J. Mater. Sci.: Mater. Med.*, 2009, **20**, 1611–1618.
80 Z. Strnad, *Biomaterials*, 1992, **13**, 317–321.
81 R. Hill, *J. Mater. Sci. Lett.*, 1996, **15**, 1122–1125.
82 R. Mathew, B. Stevensson, A. Tilocca and M. Edén, *J. Phys. Chem. B*, 2014, **118**, 833–844.
83 I. Lebecq, F. Désanglois, A. Leriche and C. Follet-Houttemane, *J. Biomed. Mater. Res., Part A*, 2007, **83A**, 156–168.
84 M. Edén, *J. Non-Cryst. Solids*, 2011, **357**, 1595–1602.
85 N. Mascaraque, M. Bauchy, J. L. G. Fierro, S. J. Rzoska, M. Bockowski and M. M. Smedskjaer, *J. Phys. Chem. B*, 2017, **121**, 9063–9072.
86 X. Lu and J. Du, *J. Non-Cryst. Solids*, 2020, **530**, 119772.
87 G. Lusvardi, G. Malavasi, F. Tarsitano, L. Menabue, M. Menziani and A. Pedone, *J. Phys. Chem. B*, 2009, **113**, 10331–10338.
88 A. Pedone and M. C. Menziani, *Molecular Dynamics Simulations of Disordered Materials*, Springer International Publishing, 2015, pp. 113–135.
89 A. Pedone, X. Chen, R. G. Hill and N. Karpukhina, *J. Phys. Chem. B*, 2018, **122**, 2940–2948.